Clemson University

TigerPrints

| Publications | Glenn Department of Civil Engineering |

8-2019

The influence of incorporation of Mn on the pitting corrosion performance of CrFeCoNi High Entropy Alloy at different temperatures

H. Torbati-Sarraf
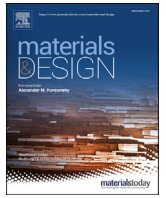
Mitra Shabani

Paul D. Jablonski

Garrett J. Pataky

A. Poursaee

The influence of incorporation of Mn on the pitting corrosion performance of CrFeCoNi High Entropy Alloy at different temperatures

H. Torbati-Sarraf [a, *], Mitra Shabani [b], Paul D. Jablonski [c], Garrett J. Pataky [b], A. Poursaee [a, d]

[a] Glenn Department of Civil Engineering, Clemson University, Clemson, SC, USA
[b] Department of Mechanical Engineering, Clemson University, Clemson, SC, USA
[c] National Energy Technology Laboratory, Albany, OR, USA
[d] Department of Materials Science and Engineering, Clemson University, Clemson, SC, USA

HIGHLIGHTS

- Incorporation of Mn into CrFeCoNi impairs corrosion resistance of the solid solution.
- The CPT for CrMnFeCoNi was much lower than that of CrFeCoNi.
- Pits on the surface of the CrMnFe-CoNi were larger and deeper than those on CrFeCoNi.
- Alternative EIS data representation provides accurate information about corrosion.

GRAPHICAL ABSTRACT
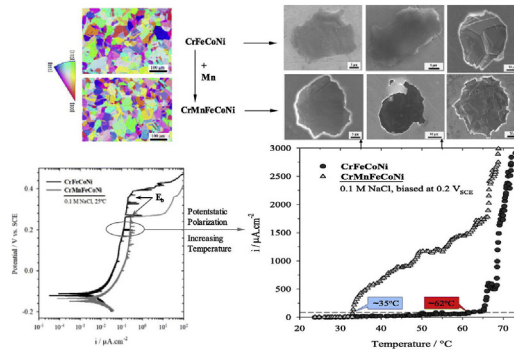
ARTICLE INFO

ABSTRACT

The electrochemical behavior and susceptibility to pitting corrosion of CrFeCoNi and CrMnFeCoNi high entropy alloys were studied in a 0.1 M NaCl solution at temperatures ranging from 25 to 75 °C. Electrochemical measurements revealed that CrMnFeCoNi is more susceptible to oxide film breakdown and localized corrosion compared to CrFeCoNi. Post corrosion microscopic observations showed severe pitting corrosion for CrMnFeCoNi in higher temperatures compared to CrFeCoNi. Based on in-depth XPS profile measurements on the remaining oxide films, this behavior was attributed to the depletion of Cr in the oxide film and detrimental presence of Mn in the matrix solid solution of CrMnFeCoNi.

1. Introduction

High-entropy alloys (HEA) were first introduced by Yeh et al. in 1995 [1,2] and are regarded as one of the most significant breakthroughs in alloying theory during recent decades [3–6]. Compared with conventional alloys which have been developed around a 'base element' model, HEAs are designed around multiple principal elements with equimolar or near equimolar elemental fractions. Because of the high mixing entropy effect [7], HEAs form disordered solid solutions instead of complex phases or intermetallic compounds [8–14]. HEAs are characterized by unusual

* Corresponding author.
   E-mail address: storbat@g.clemson.edu (H. Torbati-Sarraf).

combinations of properties not commonly found in conventional alloys, such as irradiation stability [15,16], wear [17] and hydrogen embrittlement resistance [18–20], and exceptional fracture toughness at high and cryogenic temperatures [4,8,21,22]. In addition, most HEAs contain corrosion resistant and passivating elements, such as Cr, Ti and Al [23–27] and tend to be free of common corrosion-initiation sites such as impurities and inclusions. Such versatility of HEAs makes them appropriate candidates for practical corrosion and oxidation resistant applications in form of bulk or coating materials [28–33]. However, like other conventional alloys, the alloying elements in HEAs may improve a certain property but can, unintentionally, have a negative influence on other properties [8,11,34–39].

Numerous comparative studies have been conducted between corrosion properties of HEAs and their commercially available and well-established counterpart alloys [25,31]. Chen et al. [40] reported that $Cu_{0.5}NiAlCoCrFeSi$, similar to stainless steel (SS) 304, was not susceptible to pitting in chloride-free solution, but was less resistant to localized corrosion in chloride contaminated environments. It was also shown that corrosion resistance of SS 304 exceeds that of $Al_xCrFe_{1.5}MnNi_{0.5}$ (x = 0, 0.3 and 0.5) in 0.1 N HCl. However, anodic treatment of the $Al_xCrFe_{1.5}MnNi_{0.5}$ in 15% H_2SO_4 can significantly improve the protectiveness of the oxide layer formed on its surface and consequently its corrosion resistance compared to SS 304 [41]. Qiu et al., [29] suggested that incorporation of Ti_x (x ≤ 1.5) in $Al_2CrFeNiCoCu$ cladded coating promotes the formation of a body centered cubic (BCC) crystal structure and enhances wear and corrosion resistance of Q235 steel in 0.5 M HNO_3 solution. In contrast, the addition of Ti_x and Si_x (x ≤ 1) to BCC structured $Al_{0.3}CrFe_{1.5}MnNi_{0.5}$, formed intermetallic phases and adversely affected its corrosion performance compared to SS 304 L in 3.5%wt NaCl solution [30].

Among the face centered cubic (FCC) structured HEAs, equiatomic CrMnFeCoNi, which was introduced by Cantor et al. [11], has promising mechanical properties at cryogenic and high temperatures [12,42–47]. Similar to BCC structured HEAs, CrMnFeCoNi has comparable corrosion behavior to SS 304 L in chloride-free H_2SO_4 solution, but is still susceptible to pitting corrosion in a chloride contaminated environment [28,48]. In addition, gradual removal of Cr from CrMnFeCoNi in acidic sodium chloride solution changed the process of metal dissolution from localized to general corrosion due to the formation of an imperfect Cr-rich passivation film [49]. Hsu et al. investigated the effect of Cu_x (x = 0.5, 1) in the CrFeCoNi. Their results indicated that Cu is segregated at the interdendrites and lead to passive film fragmentation [50]. Similarly, it was shown that the addition of Al to CrFeCoNi, exacerbated the localized corrosion [51,52]. The complex chemistry of HEAs may have either positive or negative ramifications on corrosion performance. This depends on the local processes such as the formation of the micro galvanic cell due to the elemental segregation or intermetallic compounds during the manufacturing process, and/or formation of a deficient passivating film [21,32,48–56].

The pitting resistance equivalent number (PREN) provides an empirical relative estimation of pitting corrosion resistance for Fe-Cr-Ni and Ni-based alloys based on experimental fitting of pitting corrosion potentials and temperatures when exposed to aqueous NaCl [57]. This number considers the most beneficial common pitting corrosion resistant alloying elements and is roughly calculated by PREN = wt%Cr + 3.3 wt% Mo + 1.6 wt% W + 16 wt% N [53,57]. Accordingly, the higher values of PREN yield higher pitting corrosion resistance. It was shown that single phase HEAs with PRENs comparable to commercial stainless steel alloys can potentially be designed for higher pitting corrosion resistance [33]. CrMnFeCoNi and CrFeCoNi alloys as single phase FCC HEAs have PRENs close to many austenitic stainless steel alloys. However, susceptibility to pitting temperature, composition and electrochemical characteristics of these concentrated solid solution alloys in chloride contaminated solutions are still unknown [26].

Furthermore, one of the key components for describing the onset of pitting corrosion and PREN is temperature and is a common parameter for screening stainless steel alloys [23,58–68]. The critical pitting temperature (CPT), first introduced by Brigham and Tozer in early 1970s [69,70], is defined as the lowest temperature at which a surface suffers from pitting corrosion.

The main objective of this study was to identify the effect of incorporating an equiatomic amount of Mn as an entropy multiplier on the corrosion performance of the CrFeCoNi based alloy using various electrochemical tests. Corrosion behavior of the CrFeCoNi and CoCrFeMnNi in 0.1 M NaCl aqueous solutions at different temperatures were investigated by polarization and electrochemical impedance spectroscopy (EIS) techniques. CPTs for both HEAs were also measured as an indication of their resistance to pitting corrosion. In addition, the morphology of the pits and the composition of the oxide film were examined using scanning electron microscopy (SEM). The formed oxide films during potentiostatic corrosion test were characterized by X-ray photoelectron spectroscopy (XPS) and relevant publications were briefly reviewed to provide more insight about the mechanism of corrosion.

2. Experimental procedures

2.1. Material preparation

The pure equiatomic CrFeCoNi and CrMnFeCoNi were melted and cast in a vacuum induction furnace. In order to reduce the residual stress and chemical inhomogeneities across dendrite arms, ingots were treated with a homogenization process at 1100 °C for 1 h, 1180 °C for 3 h and 1200 °C for 5 h. Afterward, the materials were heated to 800 °C for 3 h and wrapped in stainless steel foil pouches. Hot working including upset forging, step flattening and squaring, shaped the ingots to the final thickness of 10 mm after hot rolling. In-depth discussion of the manufacturing, calculation and characterization process can be found in [45]. The chemical compositions (wt%) of the two alloys acquired from the X-ray fluorescence (XRF) technique are listed in Table 1.

For the electrochemical experiments, 20 mm × 15 mm × 3 mm samples were cut from the ingots using electrical discharge machining. They were wet abraded sequentially from 240 to 1200 grit using SiC paper followed by light polishing with 1 μm alumina powder, washed with 50% ethanol diluted with distilled water and then dried immediately with blowing cool air. All surfaces on each sample, including the connection point, were sealed with a UV curing epoxy leaving a 1 cm^2 circular area on one side which was used as the exposed surface to the solution. Three replicates for each material were prepared for each electrochemical test. Before and after each electrochemical test, samples were examined under microscope to ensure perfection of the coating.

2.2. Electrochemical methods

All electrochemical experiments were performed in a 0.1 M NaCl aqueous solution using a conventional three-electrode cell arrangement, consisting of a saturated calomel electrode (SCE) as the reference electrode, a Pt gauze electrode as the counter

Table 1
Compositions of the alloys used in this study (wt%).

Element	Mn	Cr	Ni	Co	Fe
CrFeCoNi	0	22.8	26.4	25.47	25.11
CoCrFeMnNi	19.6	19.37	21.32	21.47	18.15

electrode and the sample as the working electrode.

Potentiodynamic polarization measurements were conducted at room temperature. The scan rate was set to 0.005 V.s^{-1} and was started from 0.01 V below the open circuit potential to the anodic potential of +0.5 V vs. SCE. The results of this test were used to estimate the passive film breakdown potential, E_b, of each alloy which was used for conducting the tests for measuring the CPT for each alloy.

The CPT of the alloy was determined by applying the anodic potential of +0.2 V vs. SCE, which was lower than the E_b at lower temperatures, and increasing the temperature from 25 °C to 75 °C at the rate of 0.6 °C/min. The temperature associated with 1 A.m^2 (100 μA.cm^{-2}) [71] was reported as the CPT. It should be mentioned that this technique was used as potentiostatic electrochemical test to compare the pitting temperature of CrFeCoNi and CrMnFeCoNi.

EIS tests were also carried out at room temperature from 25 °C to 75 °C with a 10 °C increment. Before the EIS test, each sample was charged by a DC offset potential of +0.2 V vs. SCE for 1 h. The EIS test was then started at the same potential using the 10 mV AC sinusoidal perturbation potential with the frequency ranged from 100 kHz to 50 mHz with 6 frequencies per decade.

2.3. Microstructural and compositional methods

The microstructures and the compositions of the alloys were characterized by X-ray mapping and electron backscatter diffraction (EBSD) using a Hitachi SU6600 SEM operating at 20 kV. The X-Max detector, made by Oxford Instruments, collected diffraction patterns with step size of 1 μm and analyzed using Aztec software. Prior to analysis with EBSD, both HEA pristine samples were further vibro-polished with 0.6 μm colloidal silica using a Buehler Vibromet 2. Post corrosion observations were carried with the same scanning electron microscope and parameters.

The compositions of the oxide films formed on the alloys after the CPT tests were measured by using a PHI 5000 VersaProbe III Scanning ESCA Microprobe in conjunction with monochromatic Al Kα radiation. After background subtraction, the XPS spectra were analyzed and the peaks were fitted with Gaussian functions using commercial software. The reference binding energy scale was calibrated on the C1s peak (285 eV), and all the other peaks obtained were analyzed accordingly. In-situ Ar$^+$ sputtering with various times of sputtering was used to characterize the depth profile of the elements on the corroded surface.

3. Results and discussion

3.1. Microstructural observations

Fig. 1(a$_1$, b$_1$) shows the EBSD orientation maps of the CrFeCoNi and CrMnFeCoNi alloys respectively. Both materials exhibited recrystallized FCC microstructures with high amounts of annealing twins. The average grain sizes were 21.84 μm and 23.87 μm for CrFeCoNi and CrFeCoNi respectively. These results were consistent with previous investigations [12,13,44,72,73], implying that the thermo-mechanical process applied in this study was appropriate to achieve a fully equiaxed microstructure. Fig. 1(a$_2$, b$_2$) presents the image quality and EDS mapping results. In both alloys, no element segregation or clustering was detected in the morphology, and all the alloying elements were distributed evenly in the matrix.

3.2. Electrochemical analysis

Fig. 2 shows the typical potentiodynamic polarization curves for the alloys used in this study. Generally, the corrosion potential, E_{corr}, of the CrFeCoNi was nobler than that of the CrMnFeCoNi, however in anodic branches the electrochemical responses became distinct where passive films prevented continuous dissolution of the surface. Current spikes are attributed to the formation and repassivation of metastable pits [63,74]. Further increase in the anodic overpotential gradually increased the magnitude and numbers of the metastable pits for both alloys. The averages, from three measurements, of the passivation breakdown potential, E_b, where the current abruptly and continuously increased, were approximately 0.39 and 0.28 V vs SCE for CrFeCoNi and CrMnFeCoNi, respectively. Lower values of passive current and higher values of E_b evidently show the superior corrosion resistance of CrFeCoNi and distinct protection of surface oxide film against localized corrosion compared to CrMnFeCoNi.

To investigate the influence of temperature on the corrosion behavior of the alloys and to determine the comparative CPT of these alloys, the samples were polarized and held at +0.2 V vs. SCE, which was lower than their E_b for both alloys at room temperature. By holding the samples at this potential and continuously increasing the temperature, the breakdown of the passive film and the formation of stable pits versus temperature were recorded and the CPT was determined [75].

Fig. 3 shows the results of the CPT tests for both alloys in 0.1 M NaCl solution. The threshold pitting current density, i.e. 1 A.m^2 (100 μA.cm^2), was achieved in the very early stage for the CrMnFeCoNi at around 35 °C. However, the CrFeCoNi alloy reached this threshold at 62 °C. By increasing temperature beyond the CPT, the current densities corresponding to the CrMnFeCoNi gradually increased while a relatively sharp jump was observed in the current density beyond the CPT for the CrFeCoNi.

Fig. 4 presents the Nyquist plots at different temperatures of both alloys which were anodically polarized at +0.2 V vs SCE for 1 h. Considering the axes scale of the two plots, in general, the CrFeCoNi alloy showed comparable impedance at each temperature compared to the CrMnFeCoNi alloy. All the Nyquist spectra exhibited a depressed semicircle capacitance loop followed by an obscured inductance behavior at lower frequencies. This observation suggested the characteristic of an electrochemical response from oxide film and an incomplete localized electro-dissolution or repassivation of the oxide film. The later behavior originated from the formation of surface species which change surface coverage negatively with potential alternations [76]. This behavior was previously reported for anodically charged Fe-Cr-Ni based alloys, and was attributed to the adsorption/desorption of Cr/Fe intermediate hydroxides [24,28,77,78].

Based on the described mechanism, an equivalent electrical circuit, depicted in Fig. 5, can be attributed to interface interaction.

R_s is the electrolyte resistance and can be estimated by extrapolating the high frequency asymptote line to the real axis in Nyquist plot for each temperature. R_t-Q corresponds to the high frequency impedance and ascribes the charge transfer and oxide film behavior. In the case of a non-linear surface impedance distribution and the inhomogeneity of surface reaction, the non-ideal capacity for the real system is defined as a constant phase element, Q, [76,79]. Accordingly, the corresponding impedance can be written as [80,81]:

$$Z_{CPE} = 1/Q(j\omega)^{\alpha} \qquad (1)$$

where, j and ω are an imaginary unit and angular frequency (2πf), respectively. α corresponds to a CPE exponent which attributes to cell geometry and distribution of time constant normal-to-surface [79,82]. For low frequencies, the obscured spectrum is attributed to the relaxation process, thus a R_L in series with L is added into the model, of which R_L is the resistance and L denotes the pseudo-inductance associated with partial active area relating to the localized active dissolution and incubation period for pitting [83–85].
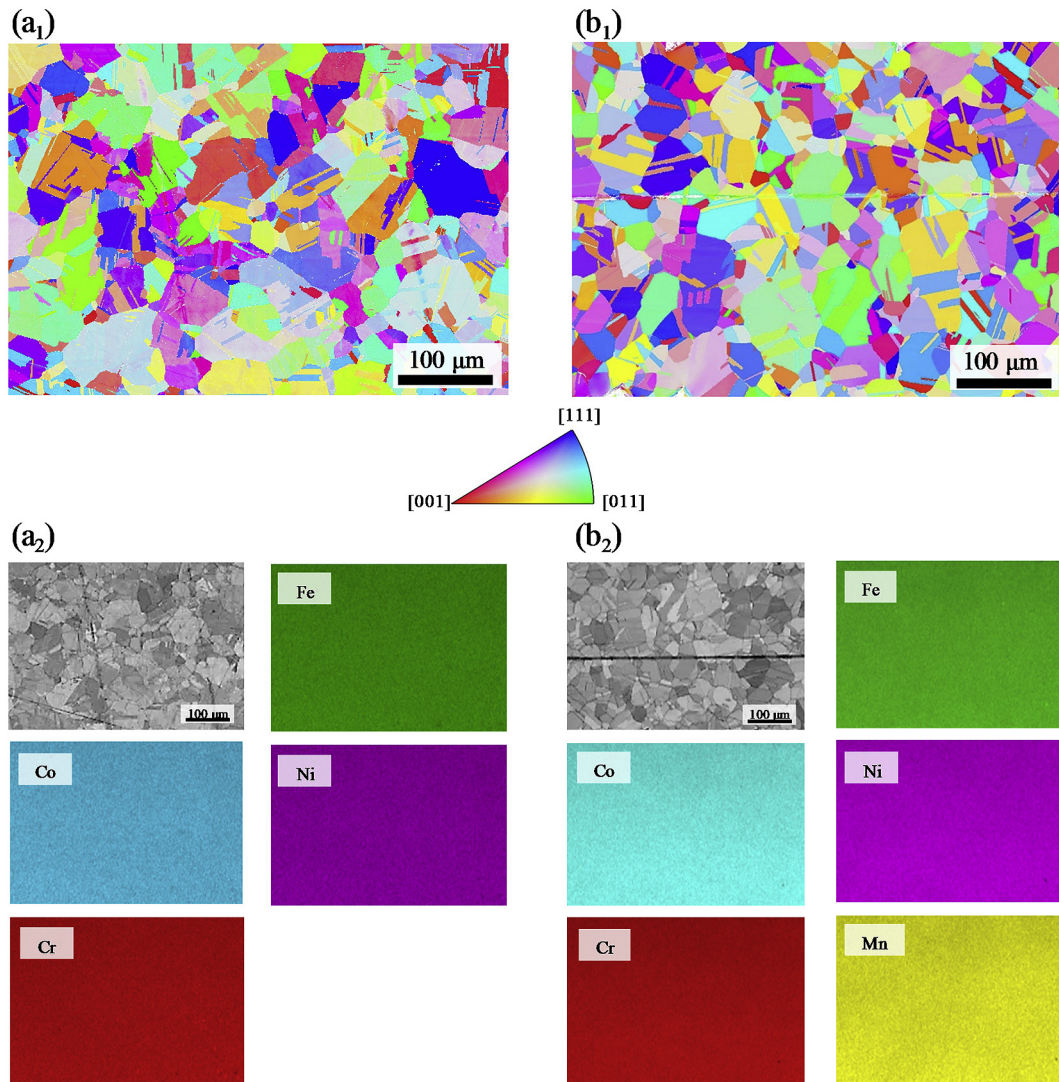
Fig. 1. (a₁, b₁) EBSD, (a₂, b₂) image quality and X-ray mapping of the CrFeCoNi and CoCrFeMnNi alloys, respectively. Colored stereographic triangle shows the plane normal directions.
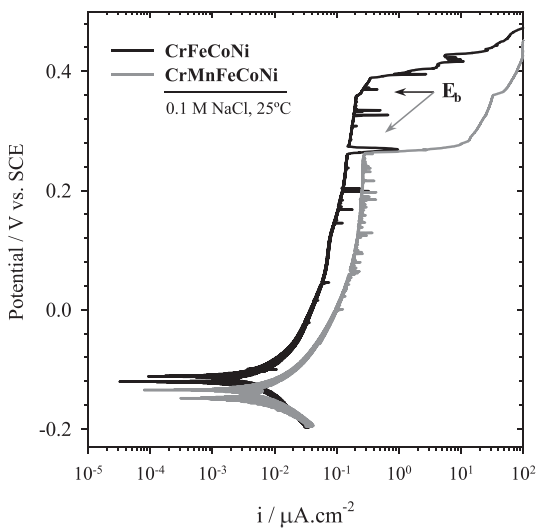

Fig. 2. Typical potentiodynamic polarization plots of CrFeCoNi and CrMnFeCoNi alloys in 0.1 M NaCl solution at room temperature.
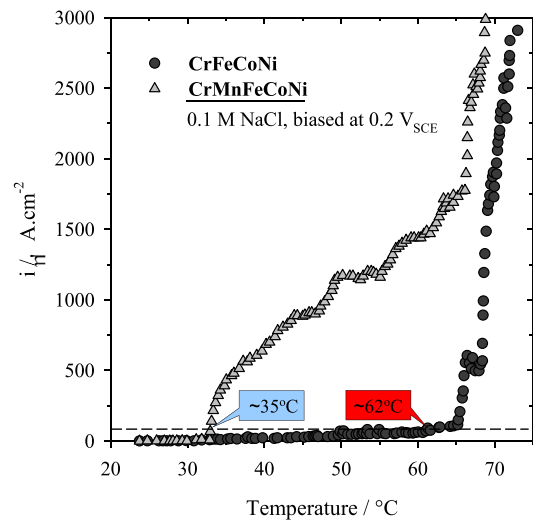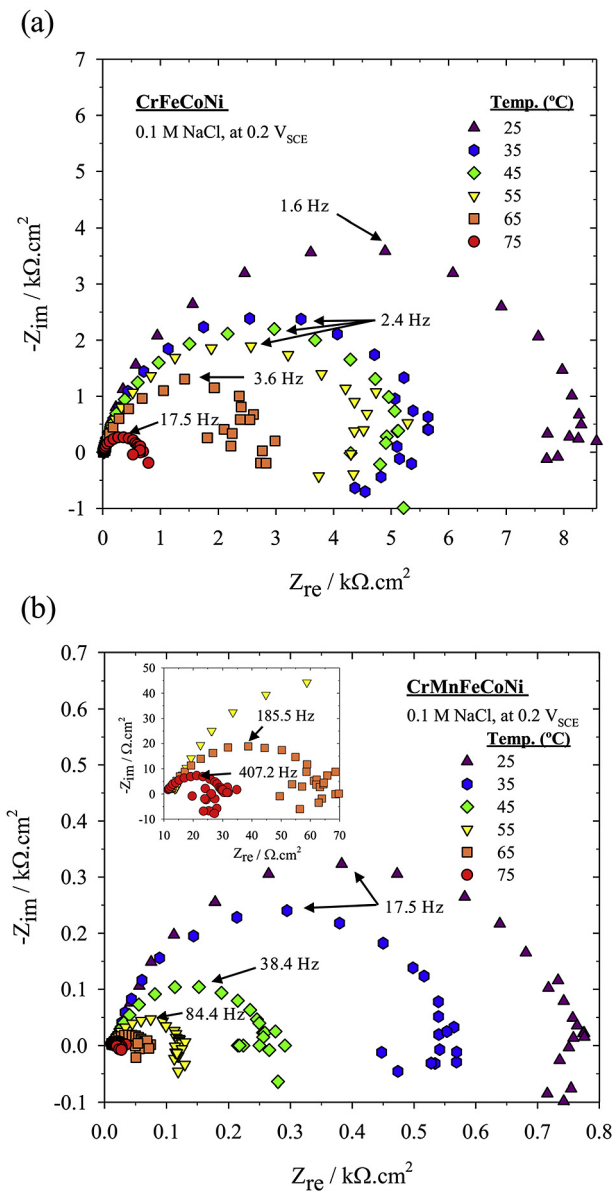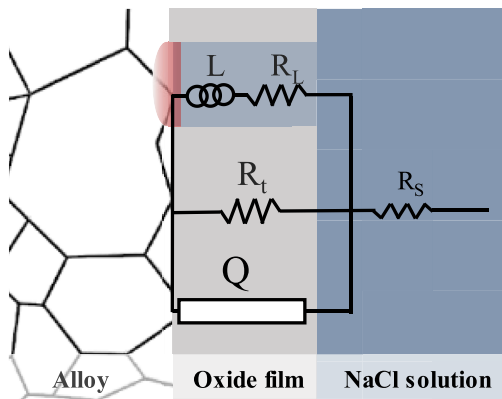
Fig. 3. CPT experimental results for the potentiostatic polarization of CrFeCoNi and CrMnFeCoNi alloys at +0.2 V vs. SCE in 0.1 M NaCl solution.

(a)

(b)

Fig. 4. Typical Nyquist plots of (a) CrFeCoNi and (b) CrMnFeCoNi obtained from the biased samples at +0.2 V vs. SCE in 0.1 M NaCl solution at different temperatures. The insert in (b) shows the early part of the Nyquist plot.

Fig. 5. Equivalent circuit and schematic representation of the interface reactions observed in the EIS spectrum for CrFeCoNi and CrMnFeCoNi in 0.1 M NaCl at various temperatures in biased potential of +0.2 V vs. SCE.

In this study, since the whole semicircles of the Nyquist plots were obtained, using graphical methods provides more realistic, with less error, interpretation and relevant physical parameters of impedance data compared to the simulation. Phase angle, φ, and impedance modulus, |Z| , were corrected for the ohmic resistance using the following equations [86] and were presented in Fig. 6 for both alloys at different temperatures:

$$|Z|_{adj} = \sqrt{(Z_{re} - R_s)^2 + Z_{im}^2} \qquad (2)$$

$$\Phi_{adj} = tan^{-1}\left(\frac{Z_{im}}{Z_{re} - R_s}\right) \qquad (3)$$

As shown, in Fig. 6, for both alloys, |Z| decreased with increase in temperature, especially at lower frequencies. Drops in impedances are most likely due to more active dissolution and facile charge transfer at the surface. In log-log Bode plots, when the |Z| responses linearly with frequency, and phase angle is relatively constant, CPE behavior reflects oxide film electronic properties [87]. For CrFeCoNi, this trend was seen in a range of 20 to 10^4 Hz which ultimately truncated by increasing the temperature over 65 °C. This drop was attributed to increasing inhomogeneous distribution of time constants along the surface due to an increase in the number and size of surface defects [80,88].

It was hypothesized that the active dissolution of pits along the surface was the reason for such behavior. For CrMnFeCoNi, the constant range of phase angles shrunk to 200 to 2×10^3 Hz for 25 and 35 °C testing temperatures and gradually obviated at the higher temperatures. This observation corroborates well with the potentostatic results for both alloys when established pits contribute to increasing current densities after the critical pitting temperature. However, in very high frequencies (higher than critical frequencies), even for low temperatures, the phases were not constant. This observation originated from the geometry-induced inhomogeneous distribution of current and potential along the surface [89,90].

In order to highlight the CPE physical features of the oxide layer, the effective CPE exponents for each spectrum was estimated from a range of frequencies as described above by using Eq. (4) [79]:

$$\alpha = \left|\frac{d(log|Z_{im}|)}{d(logf)}\right| \qquad (4)$$

Then, the effective CPE at each temperature was obtained for both alloys as [86]:

$$Q_{eff} = \frac{-1}{Z_{im}\omega^\alpha}sin\left(\frac{\pi}{2}\alpha\right) \qquad (5)$$

The graphically obtained values of R_t and effective CPEs for each temperature are reported in Table 2. For CrFeCoNi, r_t and Q_{eff} values remained relatively constant from 35 °C to 55 °C. A similar trend was observed in the CPT experiments in Fig. 3, where anodic current densities varied slightly in this range. It is well established that with the incorporation of Co and Cr in Ni-based alloys, both the stacking fault energy and point defect migration increase with an increase of temperature [91–93]. It can be hypothesized that by increasing temperature from 35 °C to 55 °C, surface annihilation is retarded by further migration of beneficial passivating element i.e. Cr interstitials or oxygen vacancies and the formation of a protective oxide film. However, with a further increase of temperature, R_t declined due to localized attack of chloride. In contrast, for the CrMnFeCoNi, same as previously shown in the CPT test, charge transfer resistances decreased continuously with increasing temperature. Although, incorporation of Mn in CrFeCoNi may increase defect migrations [16,94], the formed oxide film is not able to retard
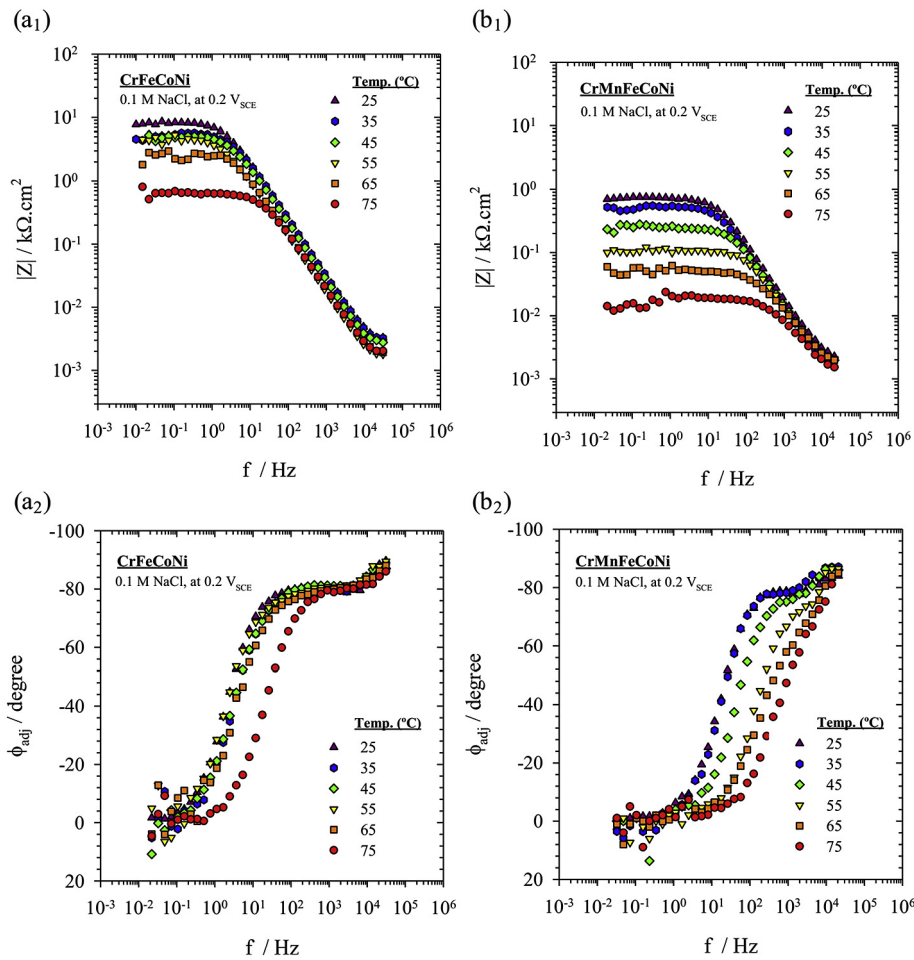
Fig. 6. Corrected (a_1,b_1) Bode and (a_2,b_2) Bode-Phase plots representation of EIS data obtained from the biased samples at +0.2 V vs. SCE in 0.1 M NaCl solution at different temperatures for CrFeCoNi and CrMnFeCoNi HEAs.

Table 2

R_t and CPE parameters obtained from graphical evaluation of EIS data at various temperatures for CrFeCoNi and CrMnFeCoNi HEAs in 0.1 M NaCl solution at 0.2 V vs. SCE.

Temperature (°C)	CrFeCoNi			CrMnFeCoNi		
	R_t (kΩ.cm^{-2})	Q_{eff} (μF.cm^{-2}.s$^{1-\alpha}$)	α	R_t (kΩ. cm^{-2})	Q_{eff} (μF.cm^{-2}.s$^{1-\alpha}$)	α
25	8.350	26.9	0.87	0.770	38.8	0.82
35	5.590	28.2	0.86	0.540	60.7	0.81
45	4.820	33.0	0.86	0.292	72.4	0.72
55	4.510	33.9	0.85	0.143	142.1	0.70
65	2.730	58.6	0.82	0.074	–	0.60
75	0.650	77.3	0.80	0.032	–	0.50

surface annihilation possibly due to lack of beneficial passivation elements [95]. As a result, the surface dissolved continuously with increasing temperature. Similarly, a drastic decrease in values of α beyond the pitting temperature is interpreted as evidence for increasing surface inhomogeneities and defects along and through the interface [96].

It should be noted that, when the geometry-dominated frequency (f_{max}) approaches the pure CPE relaxation characteristic frequency (f_0), and $\alpha \to 0.5$, quantitative evolution of CPE parameters is prone to be truncated [89]. In this experiment, as was shown in Bode phase plots for both alloys, by increasing temperature, f_{max} moved towards f_0. As a result, CPE of the interface was affected by ionic transport due to insufficient charge transfer impedance and inhomogeneous active dissolution of pits along the surface. Therefore, increasing values of Q_{eff}, and accordingly

interface capacitance [79], can be attributed to the oxide film thinning, increasing defects and ion release into the space charge.

3.3. Post corrosion microscopic observation

Global electrochemical measurements provide quantitative information about surface reactions; however, these methods use an averaged signal of the entire surface and are not capable of providing details of the localized reaction morphologies. Thus, samples obtained from EIS measurements at selected temperatures were examined under SEM. Figs. 7, 8 and 9 show the SEM micrograph of the corroded surfaces of the CrFeCoNi and CrMnFeCoNi alloys, at 75 °C, 55 °C, and 35 °C, respectively.

At 75 °C, both alloys experienced pitting corrosion, with the CrMnFeCoNi alloy having larger and deeper pits compared to the

(a₁)

(b₁)

(a₂)

(b₂)

(a₃)

(b₃)

(a₄)

(b₄)
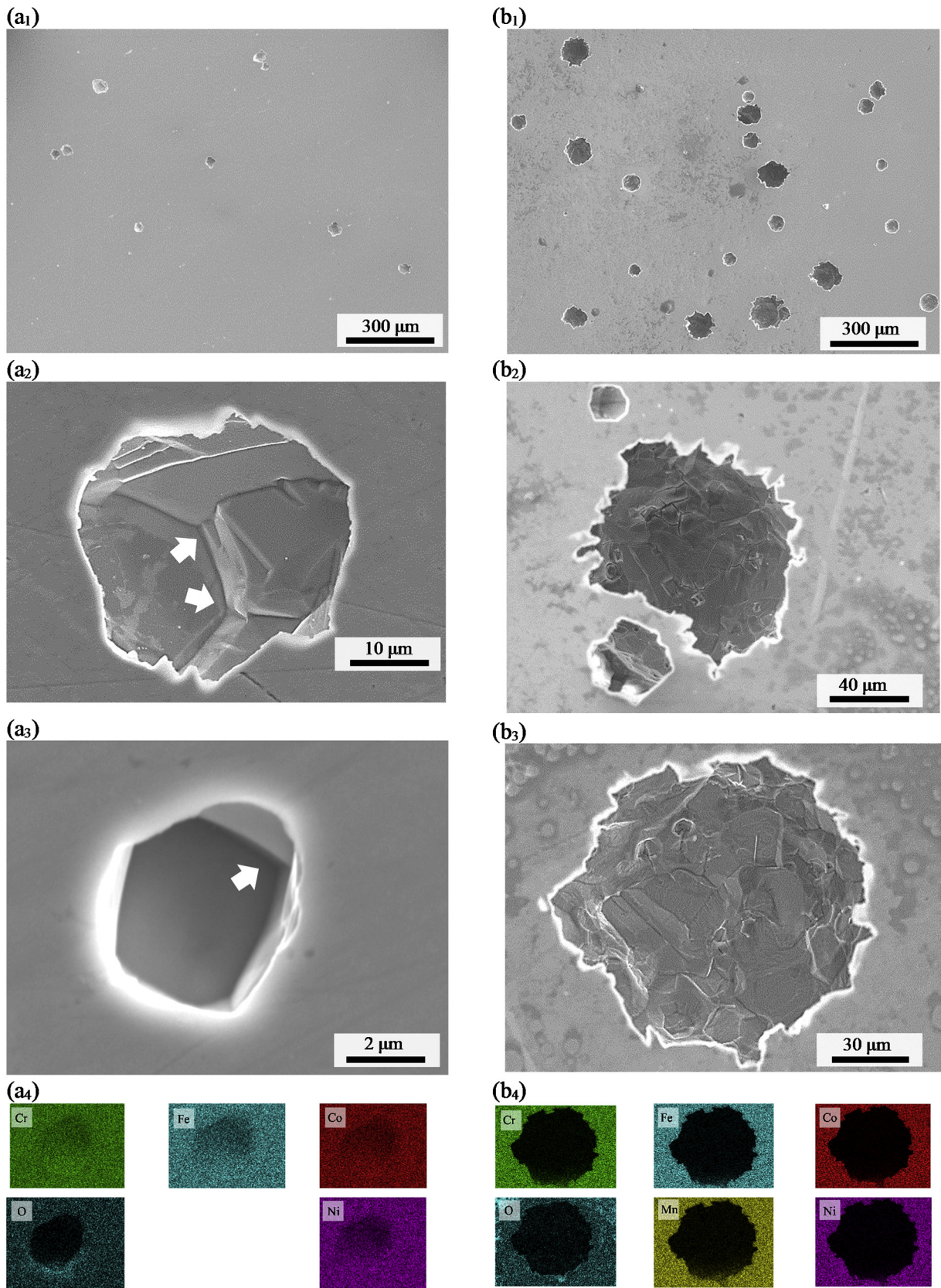
Fig. 7. Typical features of surface and pits formed at 75 °C at applied potentials of +0.2 V vs. SCE in 0.1 M NaCl on (a₁₋₃) CrFeCoNi and (b₁₋₃) CrMnFeCoNi at different magnifications. (a₄) and (b₄) elemental distribution X-ray map around pits shown in (a₃) and (b₃), respectively.
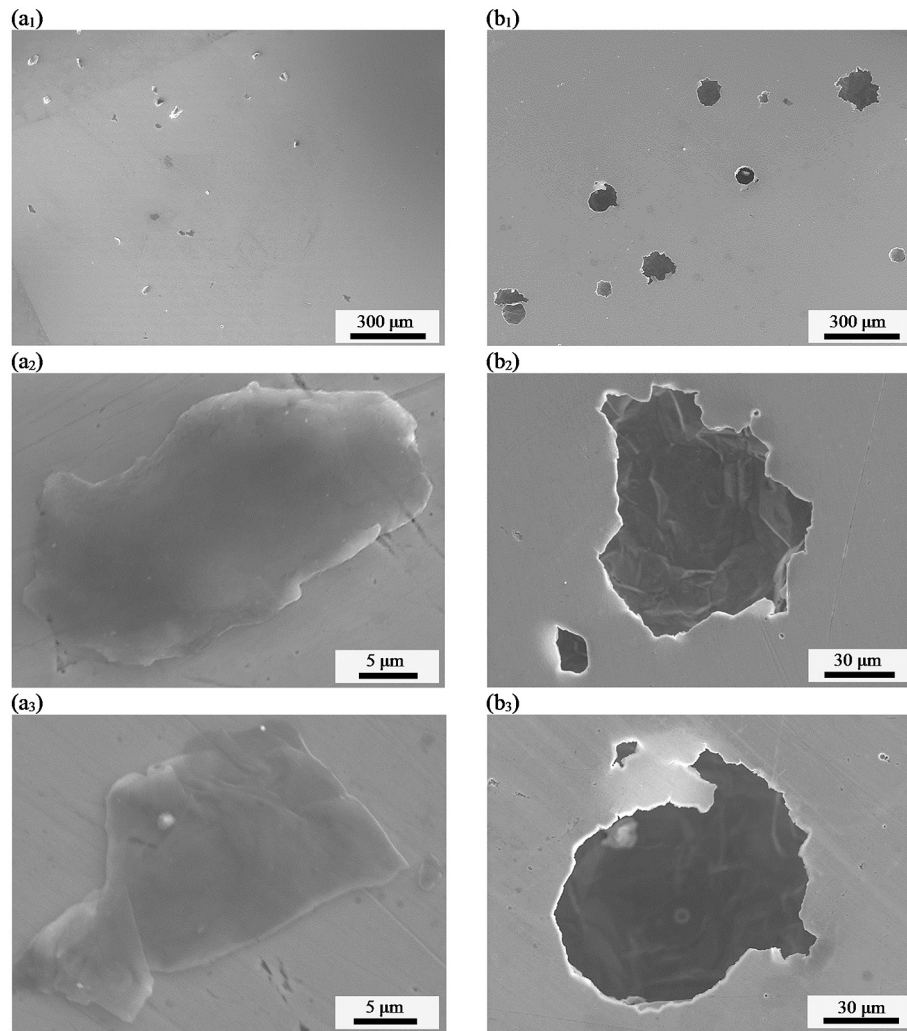
Fig. 8. Typical features of surface and pits formed at 55 °C at applied potentials of +0.2 V vs. SCE in 0.1 M NaCl on (a$_{1-3}$) CrFeCoNi and (b$_{1-3}$) CrMnFeCoNi at different magnifications.

CrFeCoNi alloy. Except at the pits, the surface of the CrMnFeCoNi alloy was attacked severely compared to that on the CrFeCoNi which is relatively intact. Elemental distribution X-ray maps around the pits showed no distinction of preferential dissolution of an alloying element. However, this measurement is considered overall as an observation; topography and depth of beam penetration may have an influence on the X-ray map resolution. At 55 °C, no discernible pitting was detected on the surface of the CrFeCoNi alloy. Localized surface demolitions were attributed to the formation of the metastable pits which passivated within a few seconds. However, deep and wide pits were observed on the surface of the CrMnFeCoNi alloy. Comparing to wide, open pits formed at 75 °C for CrMnFeCoNi, the pits mouths were still relatively covered with a crust at 55 °C (Fig. 8(b$_2$)). This metal or possibly oxide/hydroxide cover acted as a barrier and retarded the diffusion; as a result, this kept the anodic currents at lower levels at 55 °C compared to that at 75 °C. At 35 °C, no evident grown pits were detected for the CrFeCoNi alloy. However, pits were formed on the surface of the CrMnFeCoNi alloy, but relatively smaller than those formed at higher temperature counterparts. X-ray mapping analysis around the pits again revealed no preferential dissolution of a certain element due to local formation of second phase or microgalvanic cell in the matrix.

Experimental evidences and simulation results available in the literature showed that, among all these transition elements existing in examining alloy elements, incorporation of Mn in Ni matrix more efficiently facilitates defects formation and reduces vacancies migration energy [16]. As a result, voids can be formed and annihilated faster [97]. Thus, more preferential zones may provide pit nucleation sites. In contrast, by decreasing the elemental configurations, defect recombination for CrFeCoNi alloy occurred slower. As a result, void clusters enlarged [16] and dissolution may preferentially form at grain boundaries [97–101]. Concavity at grain boundaries was observed clearly in Fig. 7(a$_{2-3}$), supporting this hypothesis.

3.4. XPS results and discussion

Fig. 10 shows the in-depth XPS profiles of the alloying elements of the corroded surfaces on both alloys. XPS was conducted on the surface of the samples after the CPT test when they were anodically charged and held in the solution until 75 °C. It should be mentioned that three measurements were conducted on each corroded sample at the points that showed no effect of pitting and obtained data were consistent. Furthermore, the formed film may have partially washed away, causing the oxide/hydroxide stoichiometry to chang when removing from solution and surface contamination at the topmost layer can have a role on cation fractions. Thus, the presented results only aim to provide a comparison between the composition of the oxide film formed after the CPT tests and cannot
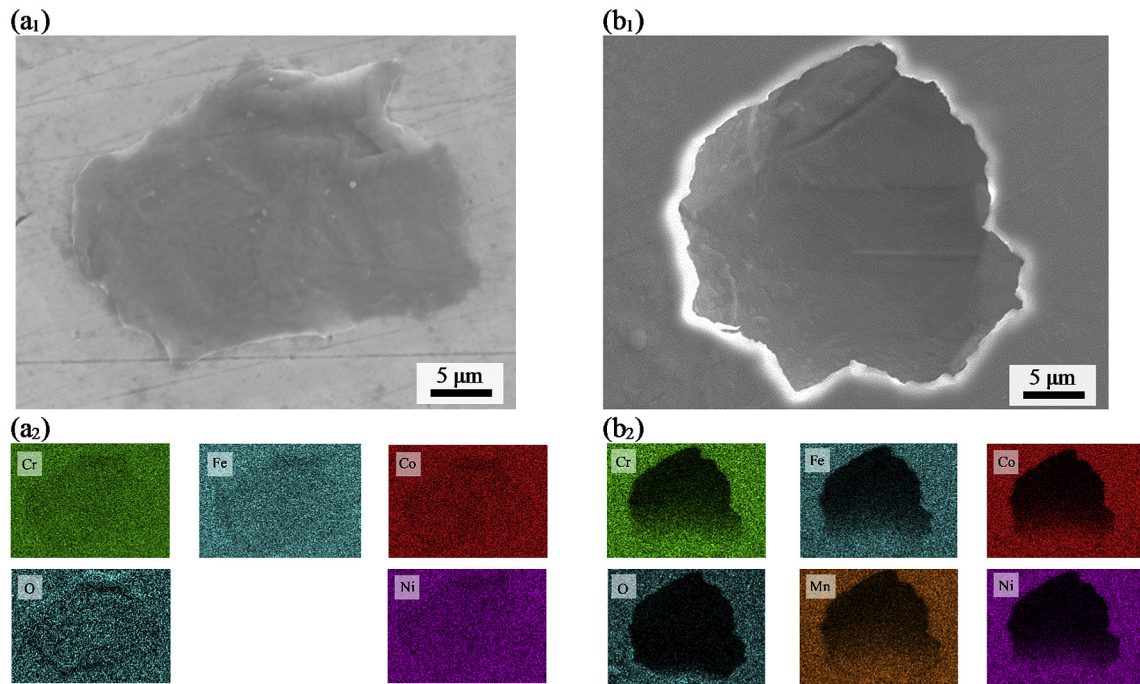
Fig. 9. Typical features and elemental distribution X-ray map around pits formed at 35 °C at the applied potentials of +0.2 V vs. SCE in 0.1 M NaCl for (a$_{1-2}$) CrFeCoNi and (b$_{1-2}$) CrMnFeCoNi.
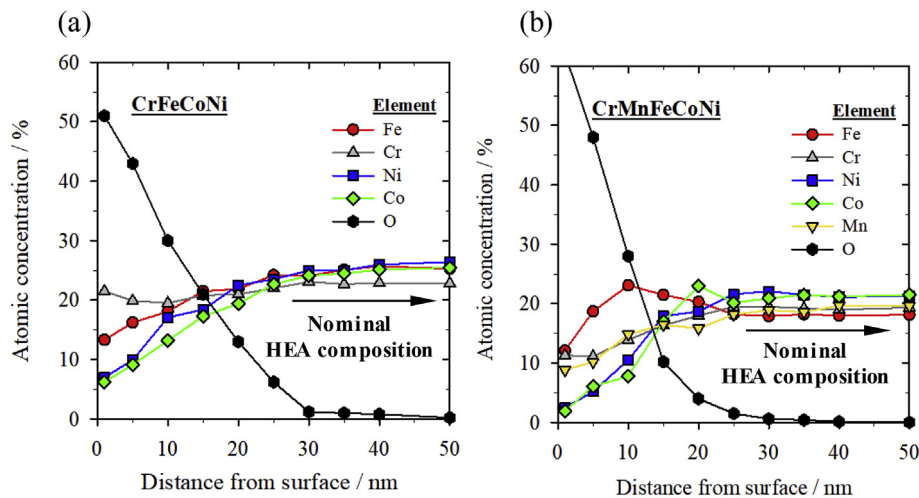
Fig. 10. Elemental composition depth profiles of the corroded surfaces of (a) CrFeCoNi (b) CrMnFeCoNi in 0.1 M NaCl after CPT test.

be considered perfect passive films.

In both cases, the concentration of the alloying elements increased, while the oxygen decreased with the increase in sputtering depth which was proportional to the depth. However, the oxygen concentration of the CrMnFeCoNi alloy at the outmost layer of the surface, i.e. the solution/outer oxide interface, was higher than that of the CrFeCoNi alloy. The greater oxygen species valency and concentration of point defects provided an easier migration path through the oxide film during the dissolution process [102−104]. It is shown that Mn decreased the vacancy migration energy and led to higher vacancy diffusion rates through the metal matrix [16] resulting in transpassivation at a lower overpotential compared to alloys without Mn [36,48,58,105−107]. Thus, on one hand, Mn can be assumed to enhance formation of defects in oxide films. On the other hand, both of the examined HEAs were

composed of 3d transition metals in which Cr and Mn have only partially filled d electrons compared to other elements which give them more electron density flexibility to contribute in charge transfer [108,109]. In contrast, Ni and Co have nearly fully-filled d electrons [36,48,102], mostly accumulated at metal/oxide interfaces. At early stage of polarization, before depassivation, Mn and Cr would favor oxide formation with higher valances, while Ni and Co dissolves without stabilized stabled oxide formation [48,94,110]. However, among all alloying elements in this study, Cr has the highest heat of adsorption of oxygen with relatively low strength of metal-metal bond, which is the key factor for nucleation of passivation [111,112]. XPS profiles showed that introducing of the Mn depleted the oxide film from Cr compounds, which leads to higher current densities during electrochemical tests. Although, the differences in bulk concentration of Cr in CrFeCoNi and

CrMnFeCoNi solid solutions is around 5 at.%, Cr concentrations at the outmost layers of CrFeCoNi is more than 10 at.% than CrMnFeCoNi, which in return, provided relatively hindrance for more oxidation and dissolution.

In addition, equiatomic additions of Mn decrease the melting point, T_m, of CrFeCoNi by more than 100 °C [113]. Hence, at a given temperature, T, the homologous temperature, i.e. T/T_m, is greater for CrMnFeCoNi and subsequently encouraged higher rates of substitutional diffusion [4,114].

Compare to Ni and Co oxides, Fe oxides have the lowest ratio of 3d correlation energy to effective initial hybridization energy which makes oxide formation easier [115]. Also, Mn increases the activity of Fe-adsorbed intermediate but reduces activity of Cr-adsorbed counterpart [107]. Accordingly, accumulation of Fe compounds at intermediate layer of oxides can be attributed to the insufficient blockage from the oxide film and higher dissolution rates of Mn and Cr with higher oxide valances. Nonetheless, characterization technique, formation of non-stoichiometric oxide solid solution, applied potentials and temperatures can potentially transform the composition profile of oxide films [102,115] and the reasoning discussed here were only qualitative.

4. Conclusions

The electrochemical and susceptibility to pitting corrosion of two equiatomic HEAs, CrFeCoNi and CoCrFeMnNi, were examined at different temperatures in 0.1 M NaCl. The main conclusions are listed below:

- CrFeCoNi showed better corrosion performance at all the examined temperatures compared to CoCrFeMnNi in the studied environment.
- Increasing temperature drastically decreased the pitting corrosion resistance of CoCrFeMnNi in comparison to CrFeCoNi.
- The poor corrosion resistance of CrMnFeCoNi in a chloride solution was attributed to the adverse effect of Mn and the lack of beneficial passivating alloying elements, i.e. Cr, on the surface.
- Generally, the pits on the surface of the CrMnFeCoNi were larger and deeper than those on the surface of the CrFeCoNi, which mostly formed at grain boundaries path.
- Based on the point defect theory of passive film, it can be hypothesized that the oxide film formed on CrMnFeCoNi was more defective than that formed on CrFeCoNi due to facile formation and migration oxygen vacancies.
- Complexity in single phase solid solution alloys in itself would not help to design a reliable and corrosion resistant HEA. Tuning appropriate alloy compositions and element concentrations based on electronic structure and oxidation resistance is a preferred method for obtaining desired properties.

CRediT authorship contribution statement

H. Torbati-Sarraf: Conceptualization, Data curation, Formal analysis, Investigation, Methodology, Visualization, Writing - original draft. **Mitra Shabani:** Data curation, Formal analysis, Investigation, Writing - review & editing. **Paul D. Jablonski:** Funding acquisition, Resources, Supervision, Writing - review & editing. **Garrett J. Pataky:** Conceptualization, Funding acquisition, Project administration, Resources, Writing - review & editing. **A. Poursaee:** Conceptualization, Resources, Software, Supervision, Validation, Writing - review & editing.

Acknowledgments

References

[1] J.W. Yeh, S.K. Chen, S.J. Lin, J.Y. Gan, T.S. Chin, T.T. Shun, C.H. Tsau, S.Y. Chang, Nanostructured high-entropy alloys with multiple principal elements: novel alloy design concepts and outcomes, Adv. Eng. Mater. 6 (2004) 299−303+274.

[2] J.W. Yeh, S.Y. Chang, Y. Der Hong, S.K. Chen, S.J. Lin, Anomalous decrease in X-ray diffraction intensities of Cu-Ni-Al-Co-Cr-Fe-Si alloy systems with multi-principal elements, Mater. Chem. Phys. 103 (2007) 41−46.

[3] S. Ranganathan, Alloyed pleasures: multimetallic cocktails, Curr. Sci. 85 (2003) 1404−1406.

[4] Y. Tang, R. Wang, S. Li, X. Liu, Y. Ye, L. Zhu, S. Bai, B. Xiao, Effect of meta-stability on non-phase-transformation high-entropy alloys, Mater. Des. 181 (2019) 107928.

[5] T. Nagase, A. Shibata, M. Matsumuro, M. Takemura, S. Semboshi, Alloy design and fabrication of ingots in Cu-Zn-Mn-Ni-Sn high-entropy and Cu-Zn-Mn-Ni medium-entropy brasses, Mater. Des. 181 (2019), 107900.

[6] J. Hou, X. Shi, J. Qiao, Y. Zhang, P.K. Liaw, Y. Wu, Ultrafine-grained dual phase $Al_{0.45}$CoCrFeNi high-entropy alloys, Mater. Des. 180 (2019), 107910.

[7] S. Singh, N. Wanderka, K. Kiefer, K. Siemensmeyer, J. Banhart, Effect of decomposition of the Cr-Fe-Co rich phase of AlCoCrCuFeNi high entropy alloy on magnetic properties, Ultramicroscopy 111 (2011) 619−622.

[8] D.B. Miracle, O.N. Senkov, A critical review of high entropy alloys and related concepts, Acta Mater. 122 (2017) 448−511.

[9] Y. Shi, B. Yang, X. Xie, J. Brechtl, K.A. Dahmen, P.K. Liaw, Corrosion of Al xCoCrFeNi high-entropy alloys: Al-content and potential scan-rate dependent pitting behavior, Corros. Sci. 119 (2017) 33−45, https://doi.org/10.1016/j.corsci.2017.02.019.

[10] Y. Zhang, T. Ting, Z. Tang, M.C. Gao, K.A. Dahmen, P.K. Liaw, Z. Ping, Micro-structures and properties of high-entropy alloys, Prog. Mater. Sci. 61 (2014) 1−93.

[11] B. Cantor, I.T.H. Chang, P. Knight, A.J.B. Vincent, Microstructural development in equiatomic multicomponent alloys, Mater. Sci. Eng. A 375−377 (2004) 213−218.

[12] M. Laurent-Brocq, A. Akhatova, L. Perrière, S. Chebini, X. Sauvage, E. Leroy, Y. Champion, Insights into the phase diagram of the CrMnFeCoNi high entropy alloy, Acta Mater. 88 (2015) 355−365.

[13] E.J. Pickering, R. Muñoz-Moreno, H.J. Stone, N.G. Jones, Precipitation in the equiatomic high-entropy alloy CrMnFeCoNi, Scr. Mater. 113 (2016) 106−109.

[14] G. Laplanche, O. Horst, F. Otto, G. Eggeler, E.P. George, Microstructural evo-lution of a CoCrFeMnNi high-entropy alloy after swaging and annealing, J. Alloys Compd. 647 (2015) 548−557.

[15] S. Zhao, Y. Osetsky, A.V. Barashev, Y. Zhang, Frenkel defect recombination in Ni and Ni − containing concentrated solid − solution alloys, Acta Mater. 173 (2019) 184−194.

[16] Z. Fan, S. Zhao, K. Jin, D. Chen, Y.N. Osetskiy, Y. Wang, H. Bei, K.L. More, Y. Zhang, Helium irradiated cavity formation and defect energetics in Ni-based binary single-phase concentrated solid solution alloys, Acta Mater. 164 (2019) 283−292.

[17] M.G. Poletti, G. Fiore, F. Gili, D. Mangherini, L. Battezzati, Development of a new high entropy alloy for wear resistance: FeCoCrNiW0.3 and FeCoCrNiW0.3 + 5 at.% of C, Mater. Des. 115 (2017) 247−254.

[18] H. Luo, Z. Li, W. Lu, D. Ponge, D. Raabe, Hydrogen embrittlement of an interstitial equimolar high-entropy alloy, Corros. Sci. 136 (2018) 403−408.

[19] Z. Pu, Y. Chen, L.H. Dai, Strong resistance to hydrogen embrittlement of high-entropy alloy, Mater. Sci. Eng. A 736 (2018) 156−166.

[20] G. Yang, Y. Zhao, D.H. Lee, J.M. Park, M.Y. Seok, J.Y. Suh, U. Ramamurty, J. il Jang, Influence of hydrogen on incipient plasticity in CoCrFeMnNi high-entropy alloy, Scr. Mater. 161 (2019) 23−27.

[21] D.H. Xiao, P.F. Zhou, W.Q. Wu, H.Y. Diao, M.C. Gao, M. Song, P.K. Liaw, Microstructure, mechanical and corrosion behaviors of AlCoCuFeNi- (Cr, Ti) high entropy alloys, Mater. Des. 116 (2017) 438−447.

[22] Y. Yin, J. Zhang, Q. Tan, W. Zhuang, N. Mo, M. Bermingham, M. Zhang, Novel cost-effective Fe-based high entropy alloys with balanced strength and ductility, Mater. Des. 162 (2019) 24−33.

[23] Y.L. Chou, Y.C. Wang, J.W. Yeh, H.C. Shih, Pitting corrosion of the high-entropy alloy Co1.5CrFeNi1.5Ti0.5Mo0.1in chloride-containing sulphate solutions, Corros. Sci. 52 (2010) 3481−3491.

[24] J.L. Polo, E. Cano, J.M. Bastidas, An impedance study on the influence of molybdenum in stainless steel pitting corrosion, J. Electroanal. Chem. 537 (2002) 183−187.

[25] Z. Tang, L. Huang, W. He, P.K. Liaw, Alloying and Processing Effects on the Aqueous Corrosion Behavior of High-entropy Alloys, 2014, pp. 895−911.

[26] Y. Qiu, S. Thomas, M.A. Gibson, H.L. Fraser, N. Birbilis, Corrosion of high entropy alloys, npj Mater. Degrad. (2017) 1−17.

[27] L. Jiang, Y. Lu, Y. Dong, T. Wang, Z. Cao, T. Li, Annealing effects on the microstructure and properties of bulk high-entropy CoCrFeNiTi0.5alloy casting ingot, Intermetallics 44 (2014) 37–43.

[28] Q. Ye, K. Feng, Z. Li, F. Lu, R. Li, J. Huang, Y. Wu, Microstructure and corrosion properties of CrMnFeCoNi high entropy alloy coating, Appl. Surf. Sci. 396 (2017) 1420–1426.

[29] X.W. Qiu, Y.P. Zhang, C.G. Liu, Effect of Ti content on structure and properties of Al2CrFeNiCoCuTixhigh-entropy alloy coatings, J. Alloys Compd. 585 (2014) 282–286.

[30] B. Ren, R.F. Zhao, Z.X. Liu, S.K. Guan, H.S. Zhang, Microstructure and properties of Al0.3CrFe1.5MnNi0.5Tixand Al$_{0.3}$CrFe$_{1.5}$MnNi$_{0.5}$Si$_x$high-entropy al-loys, Rare Metals 33 (2014) 149–154.

[31] Y. Shi, B. Yang, P. Liaw, Corrosion-resistant high-entropy alloys: a review, Metals (Basel) 7 (2017) 43.

[32] L. Wei, Y. Liu, Q. Li, Y.F. Cheng, Effect of roughness on general corrosion and pitting of (FeCoCrNi)$_{0.89}$(WC)$_{0.11}$ high-entropy alloy composite in 3.5 wt.% NaCl solution, Corros. Sci. (2018) 0–1.

[33] C.D. Taylor, P. Lu, J. Saal, G.S. Frankel, J.R. Scully, Integrated computational materials engineering of corrosion resistant alloys, npj Mater. Degrad. 2 (2018) 6.

[34] H. Torbati-Sarraf, A. Poursaee, Corrosion of coupled steels with different microstructures in concrete environment, Constr. Build. Mater. 167 (2018) 680–687.

[35] R.D. Hable, S. Alimoradi, B.S.M. Sturm, S.M. Stagg-Williams, Simultaneous solid and biocrude product transformations from the hydrothermal treat-ment of high pH-induced flocculated algae at varying Ca concentrations, Algal Res. 40 (2019), 101501.

[36] C. Lee, Y. Lee, C. Lee, S. Hong, Possibility of Mn substitution of Ni through evaluation of mechanical properties and corrosion resistance in super-austenitic stainless steel weld metal, Mater. Sci. Eng. A 733 (2018) 16–23.

[37] J.Y. He, W.H. Liu, H. Wang, Y. Wu, X.J. Liu, T.G. Nieh, Z.P. Lu, Effects of Al addition on structural evolution and tensile properties of the FeCoNiCrMn high-entropy alloy system, Acta Mater. 62 (2014) 105–113.

[38] P. Niksiar, M.B. Frank, J. McKittrick, M.M. Porter, Microstructural evolution of paramagnetic materials by magnetic freeze casting, J. Mater. Res. Technol. 8 (2019) 2247–2254.

[39] L. Ding, H. Torbati-Sarraf, A. Poursaee, The influence of the sandblasting as a surface mechanical attrition treatment on the electrochemical behavior of carbon steel in different pH solutions, Surf. Coat. Technol. 352 (2018) 112–119, https://doi.org/10.1016/j.surfcoat.2018.08.013.

[40] Y.Y. Chen, T. Duval, U.D. Hung, J.W. Yeh, H.C. Shih, Microstructure and electrochemical properties of high entropy alloys-a comparison with type-304 stainless steel, Corros. Sci. 47 (2005) 2257–2279.

[41] C.P. Lee, Y.Y. Chen, C.Y. Hsu, J.W. Yeh, H.C. Shih, Enhancing pitting corrosion resistance of AlxCrFe1.5MnNi0.5high-entropy alloys by anodic treatment in sulfuric acid, Thin Solid Films 517 (2008) 1301–1305.

[42] F. Otto, A. Dlouhý, C. Somsen, H. Bei, G. Eggeler, E.P. George, The influences of temperature and microstructure on the tensile properties of a CoCrFeMnNi high-entropy alloy, Acta Mater. 61 (2013) 5743–5755.

[43] B. Gludovatz, A. Hohenwarter, D. Catoor, E.H. Chang, E.P. George, R.O. Ritchie, A fracture-resistant high-entropy alloy for cryogenic applications, Science 345 (2014) 1153–1158 (80-.).

[44] J.J. Licavoli, M.C. Gao, J.S. Sears, P.D. Jablonski, J.A. Hawk, Microstructure and mechanical behavior of high-entropy alloys, J. Mater. Eng. Perform. 24 (2015) 3685–3698.

[45] P.D. Jablonski, J.J. Licavoli, M.C. Gao, J.A. Hawk, Manufacturing of high en-tropy alloys, Jom 67 (2015) 2278–2287.

[46] H. Shahmir, J. He, Z. Lu, M. Kawasaki, T.G. Langdon, Evidence for super-plasticity in a CoCrFeNiMn high-entropy alloy processed by high-pressure torsion, Mater. Sci. Eng. A 685 (2017) 342–348.

[47] M. Shabani, J. Indeck, K. Hazeli, P.D. Jablonski, G.J. Pataky, Effect of Strain Rate on the Tensile Behavior of CoCrFeNi and CoCrFeMnNi High Entropy Alloys, J. Mater. Eng. Perform. (7) (2019), https://doi.org/10.1007/s11665-019-04176-y in review.

[48] H. Luo, Z. Li, A.M. Mingers, D. Raabe, Corrosion behavior of an equiatomic CoCrFeMnNi high-entropy alloy compared with 304 stainless steel in sulfuric acid solution, Corros. Sci. 134 (2018) 131–139.

[49] A. Rodriguez, J.H. Tylczak, M. Ziomek-Moroz, Corrosion behavior of CoCr-FeMnNi high-entropy alloys (HEAs) under acidic aqueous conditions, Elec-trochem. Soc. 77 (2017) 741–752.

[50] Y.J. Hsu, W.C. Chiang, J.K. Wu, Corrosion behavior of FeCoNiCrCux high-entropy alloys in 3.5% sodium chloride solution, Mater. Chem. Phys. 92 (2005) 112–117.

[51] Y. Shi, L. Collins, R. Feng, C. Zhang, N. Balke, P.K. Liaw, B. Yang, Homogeni-zation of AlxCoCrFeNi high-entropy alloys with improved corrosion resis-tance, Corros. Sci. 133 (2018) 120–131.

[52] Y. Shi, B. Yang, X. Xie, J. Brechtl, K.A. Dahmen, P.K. Liaw, Corrosion of Al x CoCrFeNi high-entropy alloys: Al-content and potential scan-rate dependent pitting behavior, Corros. Sci. 119 (2017) 33–45.

[53] T. Li, O.J. Swanson, G.S. Frankel, A.Y. Gerard, P. Lu, J.E. Saal, J.R. Scully, Localized corrosion behavior of a single-phase non-equimolar high entropy alloy, Electrochim. Acta 306 (2019) 71–84.

[54] X.L. Shang, Z.J. Wang, F. He, J.C. Wang, J.J. Li, J.K. Yu, The intrinsic mechanism of corrosion resistance for FCC high entropy alloys, Sci. China Technol. Sci. 61 (2018) 189–196.

[55] Y. Qiu, S. Thomas, D. Fabijanic, A.J. Barlow, H.L. Fraser, N. Birbilis,

[56] Microstructural evolution, electrochemical and corrosion properties of Al x CoCrFeNiTi y high entropy alloys, Mater. Des. 170 (2019), 107698.

[56] Y. Cai, Y. Chen, S. Marwana, Z. Luo, F. Gao, L. Li, In fl uence of dilution rate on the microstructure and properties of FeCrCoNi high-entropy alloy coating, Mater. Des. 142 (2018) 124–137.

[57] F. Wong, The effect of alloy composition on the localized corrosion behavior of Ni-Cr-Mo alloys. http://rave.ohiolink.edu/etdc/view?acc_num=osu1237842767, 2009. (Accessed 14 June 2019).

[58] A. Pardo, M.C. Merino, A.E. Coy, F. Viejo, R. Arrabal, E. Matykina, Pitting corrosion behaviour of austenitic stainless steels - combining effects of Mn and Mo additions, Corros. Sci. 50 (2008) 1796–1806.

[59] T. Zhang, D. Wang, Y. Shao, G. Meng, F. Wang, A new criterion to determine the critical pitting temperature (CPT) based on electrochemical noise mea-surement, Corros. Sci. 58 (2012) 202–210.

[60] V.M. Salinas-Bravo, R.C. Newman, An alternative method to determine crit-ical pitting temperature of stainless steels in ferric chloride solution, Corros. Sci. 36 (1994) 67–77.

[61] S. Mehrazi, M. Saremi, J. Neshati, A probe into low-temperature stress corrosion cracking of 304L stainless steel by scanning vibrating electrode technique, Corros. Eng. Sci. Technol. 51 (2016) 358–364, https://doi.org/10.1080/1478422X.2015.1114167.

[62] M. Gholami, M. Hoseinpoor, M.H. Moayed, A statistical study on the effect of annealing temperature on pitting corrosion resistance of 2205 duplex stainless steel, Corros. Sci. 94 (2015) 156–164.

[63] N. Ebrahimi, M. Momeni, A. Kosari, M. Zakeri, M.H. Moayed, A comparative study of critical pitting temperature (CPT) of stainless steels by electro-chemical impedance spectroscopy (EIS), potentiodynamic and potentiostatic techniques, Corros. Sci. 59 (2012) 96–102.

[64] L. Jinlong, L. Tongxiang, D. Limin, W. Chen, Influence of sensitization on microstructure and passive property of AISI 2205 duplex stainless steel, Corros. Sci. 104 (2016) 144–151.

[65] W. Tian, N. Du, S. Li, S. Chen, Q. Wu, Metastable pitting corrosion of 304 stainless steel in 3.5% NaCl solution, Corros. Sci. 85 (2014) 372–379.

[66] J. Jiang, D. Xu, T. Xi, M.B. Shahzad, M.S. Khan, J. Zhao, X. Fan, C. Yang, T. Gu, K. Yang, Effects of aging time on intergranular and pitting corrosion behavior of Cu-bearing 304L stainless steel in comparison with 304L stainless steel, Corros. Sci. 113 (2016) 46–56.

[67] G.S.R. Thomas, B. Goodenough, I.D. Raistrick, R.A. Huggins, M. Tarascon, J.M. Tarascon, M.P. Technologies, L. Hutt, N. Zealand, Metastable pitting and the critical pitting temperature, Electrochem. Soc. 145 (1998) 2622–2628.

[68] M. Hoseinpoor, M. Momeni, M.H. Moayed, A. Davoodi, EIS assessment of critical pitting temperature of 2205 duplex stainless steel in acidified ferric chloride solution, Corros. Sci. 80 (2014) 197.

[69] R.J. Brigham, E.W. Tozer, Temperature as a pitting criterion, Corrosion 29 (1973) 33–36.

[70] R.J. Brigham, E.W. Tozer, Effect of alloying additions on the pitting resistance of 18% cr austenitic stainless steel, Corrosion 30 (1974) 161–166.

[71] G150-13, Standard Test Method for Electrochemical Critical Pitting Tem-perature Testing of Stainless Steels, 2004.

[72] F. Otto, A. Dlouhý, K.G. Pradeep, M. Kubĕnová, D. Raabe, G. Eggeler, E.P. George, Decomposition of the single-phase high-entropy alloy CrMnFeCoNi after prolonged anneals at intermediate temperatures, Acta Mater. 112 (2016) 40–52.

[73] B. Schuh, F. Mendez-Martin, B. Völker, E.P. George, H. Clemens, R. Pippan, A. Hohenwarter, Mechanical properties, microstructure and thermal stability of a nanocrystalline CoCrFeMnNi high-entropy alloy after severe plastic deformation, Acta Mater. 96 (2015) 258–268.

[74] Y. Tang, Y. Zuo, J. Wang, X. Zhao, B. Niu, B. Lin, The metastable pitting po-tential and its relation to the pitting potential for four materials in chloride solutions, Corros. Sci. 80 (2014) 111–119.

[75] L. Freire, X.R. Nóvoa, G. Pena, V. Vivier, On the corrosion mechanism of AISI 204Cu stainless steel in chlorinated alkaline media, Corros. Sci. 50 (2008) 3205–3212.

[76] D.A. Harrington, P. Van Den Driessche, Mechanism and equivalent circuits in electrochemical impedance spectroscopy, Electrochim. Acta 56 (2011) 8005–8013.

[77] K. Morshed-Behbahani, P. Najafisayar, M. Pakshir, M. Shahsavari, An elec-trochemical study on the effect of stabilization and sensitization heat treatments on the intergranular corrosion behaviour of AISI 321H austenitic stainless steel, Corros. Sci. 138 (2018) 28–41.

[78] J.M. Bastidas, J.L. Polo, C.L. Torres, E. Cano, Study on the stability of AISI 316L stainless steel pitting corrosion through its transfer function, Corros. Sci. 43 (2001) 269–281.

[79] B. Hirschorn, M.E. Orazem, B. Tribollet, V. Vivier, I. Frateur, M. Musiani, Determination of effective capacitance and film thickness from constant-phase-element parameters, Electrochim. Acta 55 (2010) 6218–6227.

[80] J.B. Jorcin, M.E. Orazem, N. Pébère, B. Tribollet, CPE analysis by local elec-trochemical impedance spectroscopy, Electrochim. Acta 51 (2006) 1473–1479.

[81] G.J. Brug, A.L.G. van den Eeden, M. Sluyters-Rehbach, J.H. Sluyters, The analysis of electrode impedances complicated by the presence of a constant phase element, J. Electroanal. Chem. Interfacial Electrochem. 176 (1984) 275–295.

[82] S. Cattarin, M. Musiani, B. Tribollet, V. Vivier, Impedance of Passive Oxide Films With Graded Thickness: Influence of the Electrode and Cell Geometry vol. 54, 2009, pp. 6963–6970.

[83] B. Zhao, J.-H. Li, R.-G. Hu, R.-G. Du, C.-J. Lin, Study on the corrosion behavior of reinforcing steel in cement mortar by electrochemical noise measurements, Electrochim. Acta 52 (2007) 3976–3984.

[84] T. Zhang, C.L. Zeng, Corrosion protection of 1Cr18Ni9Ti stainless steel by polypyrrole coatings in HCl aqueous solution, Electrochim. Acta 50 (2005) 4721–4727.

[85] A. Arutunow, K. Darowicki, DEIS Evaluation of the Relative Effective Surface Area of AISI 304 Stainless Steel Dissolution Process in Conditions of Intergranular Corrosion vol. 54, 2009, pp. 1034–1041.

[86] M.E. Orazem, N. Pébère, B. Tribollet, J.E. Soc, P. B-b, M.E. Orazem, N. Pébère, B. Tribollet, Enhanced graphical representation of electrochemical impedance data service enhanced graphical representation of electrochemical, J. Electrochem. Soc. 153 (2006) 128–136.

[87] S. Delaunay, J. Tireau, J. Baux, N. Causs, M. Roy, D. You, P. Nadine, Impedance Analysis of Film-forming Amines for the Corrosion Protection of a Carbon Steel r o vol. 283, 2018.

[88] B. Ballesteros, C. Gonza, P.A. Castro, A. Schulte, E.J. Cal, W. Schuhmann, Precursor Sites for Localised Corrosion on Lacquered Tinplates Visualised by Means of Alternating Current Scanning Electrochemical Microscopy vol. 48, 2003, pp. 1115–1121.

[89] P. Córdoba-torres, T.J. Mesquita, R.P. Nogueira, Influence of geometry-induced current and potential distributions on the characterization of constant-phase element behavior, Electrochim. Acta 87 (2013) 676–685.

[90] H. Torbati-Sarraf, S.A. Torbati-Sarraf, A. Poursaee, T.G. Langdon, Electrochemical behavior of a magnesium ZK60 alloy processed by high-pressure torsion, Corros. Sci. 154 (2019) 90–100.

[91] S. Zhao, G.M. Stocks, Y. Zhang, Stacking fault energies of face-centered cubic concentrated solid solution alloys, Acta Mater. 134 (2017) 334–345.

[92] S. Huang, W. Li, S. Lu, F. Tian, J. Shen, E. Holmström, L. Vitos, Temperature dependent stacking fault energy of FeCrCoNiMn high entropy alloy, Scr. Mater. 108 (2015) 44–47.

[93] S. Zhao, Y. Osetsky, Y. Zhang, Preferential diffusion in concentrated solid solution alloys: NiFe, NiCo and NiCoCr, Acta Mater. 128 (2017) 391–399.

[94] K. Lutton, K. Gusieva, N. Ott, N. Birbilis, J.R. Scully, Understanding multi-element alloy passivation in acidic solutions using operando methods, Electrochem. Commun. 80 (2017) 44–47.

[95] J. Pang, T. Xiong, X. Wei, Z. Zhu, B. Zhang, Y. Zhou, X. Shao, Q. Jin, S. Zheng, X. Ma, Oxide MnCr2O4 induced pitting corrosion in high entropy alloy CrMnFeCoNi, Materialia 6 (2019), 100275.

[96] P. Córdoba-Torres, T.J. Mesquita, O. Devos, B. Tribollet, V. Roche, R.P. Nogueira, On the intrinsic coupling between constant-phase element parameters α and Q in electrochemical impedance spectroscopy, Electrochim. Acta 72 (2012) 172–178.

[97] S. Zhao, T. Egami, G.M. Stocks, Y. Zhang, Effect of d electrons on defect properties in equiatomic NiCoCr and NiCoFeCr concentrated solid solution alloys, Phys. Rev. Mater. 013602 (2018) (2018) 1–8, 2, 013602.

[98] A. Schreiber, C. Rosenkranz, M.M. Lohrengel, Grain-dependent anodic dissolution of iron, Electrochim. Acta 52 (2007) 7738–7745.

[99] K.L. Merkle, D.J. Smith, Atomic structure of symmetric tilt grain boundaries in NiO, Phys. Rev. Lett. 59 (1987) 2887–2890.

[100] K.L. Merkle, Atomic structure of grain boundaries, J. Phys. Chem. Solids 55 (1994) 991.

[101] H. Torbati-Sarraf, A. Poursaee, Corrosion improvement of carbon steel in concrete environment through modification of steel microstructure, J. Mater. Civ. Eng. 31 (2019) 2–7.

[102] H.H. Strehblow, Passivity of metals studied by surface analytical methods, a review, Electrochim. Acta 212 (2016) 630–648.

[103] D.D. Macdonald, The point defect model for the passive state, J. Electrochem. Soc. 139 (1992) 3434.

[104] H. Torbati-Sarraf, A. Poursaee, Study of the passivation of carbon steel in simulated concrete pore solution using scanning electrochemical microscope (SECM), Materialia 2 (2018) 19–22, https://doi.org/10.1016/j.mtla.2018.08.011.

[105] H.Y. Ha, M.H. Jang, T.H. Lee, Influences of Mn in Solid Solution on the Pitting Corrosion Behaviour of Fe-23 wt%Cr-based Alloys, Elsevier Ltd, 2016.

[106] J. Robertson, The mechanism of high temperature aqueous corrosion of stainless steels, Corros. Sci. 32 (1991) 443–465.

[107] K.J. Park, H.S. Kwon, Effects of Mn on the localized corrosion behavior of Fe-18Cr alloys, Electrochim. Acta 55 (2010) 3421–3427.

[108] S. Zhao, Y. Osetsky, Local-environment dependence of stacking fault energies in concentrated solid-solution alloys, npj Comput. Mater. (2018) 1–7.

[109] L. Wang, T. Maxisch, G. Ceder, Oxidation Energies of Transition Metal Oxides Within the GGA + U Framework, 2006, pp. 1–6.

[110] K.F. Quiambao, S.J. Mcdonnell, D.K. Schreiber, A.Y. Gerard, K.M. Freedy, P. Lu, J.E. Saal, G.S. Frankel, J.R. Scully, Passivation of a corrosion resistant high entropy alloy in non-oxidizing sulfate solutions, Acta Mater. 164 (2019) 362–376.

[111] P. Marcus, On some fundamental factors in the effect of alloying elements on passivation of alloys, Corros. Sci. 36 (1994) 2155–2158.

[112] B. Lü, G. Chen, W. Zhou, H. Su, R. Liu, Ab initio study of influence of 3d alloying elements on corrosion properties of non-passivated nickel-base alloys, J. Nucl. Mater. 418 (2011) 286–291.

[113] K. Jin, C. Zhang, F. Zhang, H. Bei, Influence of Compositional Complexity on Interdiffusion in Ni-containing Concentrated Solid-solution Alloys, 2018, p. 3831.

[114] M. Vaidya, S. Trubel, B.S. Murty, G. Wilde, S.V. Divinski, Ni tracer diffusion in CoCrFeNi and CoCrFeMnNi high entropy alloys, J. Alloys Compd. 688 (2016) 994–1001.

[115] R. Zimmermann, P. Steiner, R. Claessen, F. Reinert, S. Hu, Electronic Structure Systematics of 3d Transition Metal Oxides vol. 96, 1998, pp. 179–186.